JGR Biogeosciences

RESEARCH ARTICLE
10.1029/2020JG005887

Direct-Push Color Logging Images Spatial Heterogeneity of Organic Carbon in Floodplain Sediments

Stefan Klingler[1], Olaf A. Cirpka[1], Ulrike Werban[2], Carsten Leven[1], and Peter Dietrich[1,2]

[1]Center for Applied Geoscience, University of Tübingen, Tübingen, Germany, [2]Department of Monitoring and Exploration Technologies, Helmholtz Centre for Environmental Research GmbH - UFZ, Leipzig, Germany

Key Points:
- Direct-push methods allow vertical in situ profiling of sediment color at high resolution
- Cluster analysis reproducibly delineates colorfacies indicative of sedimentary units
- Site-specific relationships between color and TOC in sediments permit identifying biogeochemical hot spots

Supporting Information:
- Supporting Information S1
- Figure S1
- Figure S2
- Figure S3
- Figure S4

Correspondence to:
O. A. Cirpka,
olaf.cirpka@uni-tuebingen.de

Citation:
Klingler, S., Cirpka, O. A., Werban, U., Leven, C., & Dietrich, P. (2020). Direct-push color logging images spatial heterogeneity of organic carbon in floodplain sediments. *Journal of Geophysical Research: Biogeosciences*, *125*, e2020JG005887. https://doi.org/10.1029/2020JG005887

Received 8 JUN 2020
Accepted 27 OCT 2020
Accepted article online 27 NOV 2020

Author Contributions:
Conceptualization: Ulrike Werban, Carsten Leven, Peter Dietrich
Formal analysis: Stefan Klingler
Funding acquisition: Olaf A. Cirpka, Carsten Leven
Investigation: Stefan Klingler
Methodology: Stefan Klingler, Peter Dietrich
Software: Stefan Klingler, Olaf A. Cirpka
Supervision: Olaf A. Cirpka, Ulrike Werban, Carsten Leven, Peter Dietrich
(continued)

Abstract In soils and sediments, large amounts of total organic carbon (TOC) mark reducing conditions. As dark sediment colors are good predictors for high-TOC zones, they indicate hot spots of biogeochemical turnover and microbial activity. Traditionally, obtaining the sediment color or TOC at depth requires costly core sampling, resulting in poor horizontal resolution and related uncertainty caused by interpolation. We suggest using a direct-push tool for optical screening of the sediment color to acquire multiple high-resolution vertical color profiles and demonstrate its applicability to a biogeochemical transition zone in floodplain sediments, dominated by tufa. We use Gaussian mixture models for a cluster analysis of 35 color logs in the International Commission on Illumination (CIE) *L*a*b** color space to identify three colorfacies that differ in lithology and TOC content: a dark colorfacies that agrees well with peat layers, a gray colorfacies associated with clay, and a creamy-brown facies made of autochthonous carbonate precipitates. We test different approaches either to infer the TOC content from color metrics, namely, the lightness and chroma, across all facies, or to identify TOC ranges for each colorfacies. Given the high variability in TOC due to organic carbon specks in the tufa, the latter approach appears more realistic. In our application we map the 3-D distribution of organic matter in a floodplain in distinct facies over 20,000 m^2 down to 12 m depth. While we relate the sediment color only to the TOC content, direct-push color logging may also be used for in situ mapping of other biogeochemically relevant properties, such as the ferric-iron content or sedimentary structure.

Plain Language Summary Geologists can say a lot about soils and loose materials in the ground by looking at their color. Dark materials normally contain dead plants, called organic carbon, which are food for bacteria and cause chemical reactions. To get the color of the soil, geologists normally need soil samples, but getting them from depth takes time and money. We test a method of pushing a camera into the ground and recording the color therein. From the recorded color we can say which type of geological material is at which depth and how much organic carbon is there without taking samples everywhere. This can be done very quickly, so that we can do it over a large area and down to the depth of the loose material in the ground, where most of the groundwater flows.

1. Introduction

Organic carbon is one of the most important electron donors in soils and sediments. Zones of high total organic carbon (TOC) content are hot spots of denitrification, iron, manganese, sulfur reduction, and methanogenesis (Bauer & Kappler, 2009; Korom, 1992; Rivett et al., 2008), with further implications on trace metal cycling (Glodowska et al., 2020; Kalbitz & Wennrich, 1998; Lawson et al., 2016; McArthur et al., 2004). In biogeochemical studies, the TOC content of soils and sediments may be predicted through its well-established relationship to dark colors (Blume & Helsper, 1987; Konen et al., 2003; Steinhardt & Franzmeier, 2008; Viscarra Rossel et al., 2006b; Wills et al., 2007). Sediment color in turn is one of the most basic, yet highly informative parameters in geoscience. It is one of the first properties described in classical field geology and sedimentology and used for soil classification in soil science. Color may indicate sediment features (Dorador & Rodríguez-Tovar, 2016), climatic and seasonal cycles in limnology and marine geology (Nederbragt & Thurow, 2001; Peterson et al., 2000; Zolitschka et al., 2015), soil fertility (Adamchuk et al., 2004; Liles et al., 2013), redox conditions (Lyle, 1983), and other soil and sediment properties (Gholizadeh et al., 2020; Hartemink & Minasny, 2014; Spielvogel et al., 2004; Viscarra Rossel et al., 2009; Waiser et al., 2007). In this study, we record the in situ sediment color by direct-push color logging to

Visualization: Stefan Klingler, Olaf A. Cirpka
Writing – original draft: Stefan Klingler
Writing – review & editing: Olaf A. Cirpka, Ulrike Werban, Carsten Leven, Peter Dietrich

demonstrate its suitability to detect and map deeper subsurface features with high TOC content (i.e., peat layers) potentially relevant to biogeochemical cycling, microbial activity, and pollutant turnover processes.

TOC measurements are commonly done on samples, taken either with a manual soil sampler or from drilling cores. While topsoil samples may be taken at high spatial resolution over large areas, gathering deeper subsurface samples by drilling is time consuming, costly, and labor intense. In most cases, only a limited number of cores, often at substantial distance to each other, can be taken. As a result, the continuity, connectivity, and geometry of potentially relevant high-TOC features cannot be resolved. If the lateral extent of the features is smaller than the distance between the cores, neither geostatistical analysis nor deterministic interpolation to construct profiles of facies distributions or individual properties of the subsurface, such as the TOC content, is possible.

A way to fill the gap between discrete sampling points and to obtain (semi)continuous information about the subsurface is by geophysical surveying. Ground-penetrating radar (Comas et al., 2017; Corradini et al., 2020), geoelectrical (Kettridge et al., 2008; Kowalczyk et al., 2017; Slater & Reeve, 2002), and electromagnetic surveys (Silvestri et al., 2019) are not sensitive to TOC directly yet have been applied to map thicknesses and layer contacts of peats and other geophysical facies with high TOC determined on core samples. However, the detectability of thin deeper layers, as well as their internal heterogeneity and stratification, suffers from strong signal attenuation at sites with a thick, conductive top layer and from rapid decrease in vertical resolution with depth (Comas et al., 2015). Alternatively, relating well-logging parameters to TOC content allow a depth-independent high vertical resolution of carbon content in petroleum geoscience (Passey et al., 1990; Zhu et al., 2020). This, however, requires costly boreholes and downhole equipment and is hence highly impractical for spatial mapping of TOC in near-surface formations. For the detection of peat layers, the use of cone penetration tests (CPT) is also suggested, as CPT results in high friction ratios and very low tip resistances (Boylan & Long, 2012; Lunne et al., 2002; Tumay et al., 2013). However, the relationship between the mechanical soil properties and TOC content is not necessarily unique, can be site specific, and may be confronted with sensitivity issues of the CPT probe in reliably acquiring the very low tip resistances expected for peat layers (Boylan & Long, 2012). That is, densely spaced in situ color profiles may be the best option for a quick and highly resolved indirect imaging of TOC content independent of depth.

A common approach of measuring color in soil science is by means of spectrophotometers or near-infrared/visual (NIR-VIS) spectral probes (Adamchuk et al., 2004; Moritsuka et al., 2019; Viscarra Rossel et al., 2006a). The color of the soil is measured on grab samples in the lab, on outcrops, or on samples under field conditions (Doetterl et al., 2013; Heil et al., 2020; Morgan et al., 2009; Zhang & Hartemink, 2019b). Alternatively, optical imaging tools have been developed to acquire in situ soil color on the ground surface (Rodionov et al., 2015), in fresh trenches of up to 20 cm depth (Aliah Baharom et al., 2015; Knadel et al., 2015), or by probes pushed down to 120 cm into the ground (Poggio et al., 2015; Veum et al., 2018; Zhang et al., 2017). The traditional color classification with Munsell color charts is hereby known to be rather subjective, because it depends on the eyesight of the researcher and the surrounding light conditions (Melville & Atkinson, 1985). Therefore, in recent years most studies report sediment color measurements from spectrophotometers, core scanners, and NIR-VIS probes in the $L^*a^*b^*$ color space of the International Commission on Illumination (CIE) (Melville & Atkinson, 1985; Viscarra Rossel et al., 2006b). This color space can be visualized in 3-D Cartesian coordinates with L^* as the lightness axis ranging from 0 (black) to 100 (white), the a^* axis ranging from green (negative) to red (positive), and the b^* axis ranging from blue (negative) to yellow (positive) (CIE, 1978). The corresponding cylindrical system of coordinates expresses the a^*b^* values as chroma C^*, representing the color saturation and the hue angle $h°$.

Relationships of sediment color in the CIE $L^*a^*b^*$ color space have been reported for iron content (Barron & Torrent, 1986; Heil et al., 2020), mineral composition (Barron & Torrent, 1986; Scheinost & Schwertmann, 1999; Torrent et al., 1983), and TOC content (Aitkenhead et al., 2013; Viscarra Rossel et al., 2006b). Most recently, cluster analyses of spectrophotometer measurements and even digital images of a soil profile wall allowed delineating soil horizons and parameter zonation solely based on color (Zhang & Hartemink, 2019a, 2019b). Promising as they are, these relationships are limited to color measurements on available outcrops, grab and core samples, as well as to the shallow depths which can be reached by the in situ probes. The ex situ approaches additionally bare color alterations during the coring, sampling, and sample-processing procedures. Many studies reported an alteration of the sample color due to changes in moisture content, mineral precipitations, or oxidation (Morgan et al., 2009; Wijewardane et al., 2020).

We see a need of in situ subsurface characterization by color at greater depth than possible by the usual grab samples and in situ probes and with higher spatial resolution than by few costly drilling cores. These requirements are met by direct-push in situ color logging, in which a rod with an outward oriented sapphire glass window is continuously advanced into the ground by standard direct-push machines. A sensor in the probe or in a surface processing unit records a defined wavelength or the entire visual spectrum of light reflected from the sediments upon illumination by a white light or a laser (Ackerson et al., 2017; Bujewski & Rutherford, 1997; Einarson et al., 2018; Hausmann et al., 2016; Kram et al., 2001; McCall et al., 2018). Sounding locations can be spaced in the low decimeter range for high horizontal resolution and executed along transects or grids with more than 100 m of probing per day (Einarson et al., 2018; Hausmann et al., 2016; McCall et al., 2018). Dalan et al. (2011), Hausmann et al. (2018), and Rabiger-Völlmer et al. (2020) used multiple vertical color logs along profiles to detect and map the geometry of archeological features based on spatial and vertical color contrasts. Similar probes have been used to detect and map contaminants and dye tracers in the subsurface (Einarson et al., 2018; Kram et al., 2001; McCall et al., 2018; Reischer et al., 2020). The vertical resolution is in the centimeter range. In contrast to drilling methods, direct-push color logging does neither suffer from alterations of the sediment color upon sampling nor from false depth allocations due to incomplete core recovery or core compaction/expansion. Direct-push color logging therefore appears a promising approach to image the spatial distribution of sediment color over several meters depth at a depth-independent resolution so far unmet by any other geophysical method.

In this study we use direct-push color logging to characterize the spatial color distribution of floodplain sediments over 165 m × 130 m × 12 m yet with a high vertical and spatial resolution. The sedimentary record consists of lithofacies in three distinct colors (gray, brown, and dark). We target the distribution of dark colored high-TOC features identified as peat lenses which are potentially relevant to the floodplain hydrogeochemistry. Hence, we perform a cluster analysis of the obtained $L^*a^*b^*$ values from 35 color logs by a Gaussian mixture model resulting in three colorfacies and construct profiles of the facies distribution. Finally, we determine a site-specific relationship between the sediment color and the sediment TOC content and assign ranges of TOC to the individual colorfacies.

2. Methods

2.1. Site Setting

We performed the direct-push color logging fieldwork in unconsolidated Quaternary floodplain sediments in the Ammer valley near Tübingen, Germany. Previous floodplain-wide distributed sediment coring indicated a sedimentary succession typical for European Pleistocene to Holocene floodplains (Dabkowski, 2020; Fuchs et al., 2011; Lespez et al., 2008; Newell et al., 2015; Žák et al., 2002): up to 10 m thick clay-rich gravels at the bottom, overlain by a 1–3 m thick silty clay, up to 8 m thick calcareous tufa sediments with abundant vegetation and organic-rich layers and an upper 2 m of silty clay alluvial cover (Martin et al., 2020). In many of these cores we found up to 1 m thick peat layers at different depths within the tufa sequence. Tufa sediments generally indicate a spatially very variable swampy depositional environment with ponding waters and patchy vegetation in warm climate (Dabkowski, 2020; Pedley, 1990). Therefore, we expected a high spatial variability of peat lenses with high organic carbon content. In the Ammer valley floodplain, the tufa sediments function as a confined regional aquifer with strong reducing conditions in the floodplain center (Martin et al., 2020). Along the fringes, however, oxic water infiltrates from the surrounding hillslopes and causes a hydrogeochemical transition zone along the floodplain boundary. As a result, we measured dissolved oxygen in monitoring wells at the hillslope and floodplain perimeter yet no dissolved oxygen, low redox potential, and elevated bisulfide concentrations in monitoring wells approximately 50 m toward the floodplain center. The width of this transition zone along the floodplain fringe may hereby be strongly influenced by the presence and extent of TOC-rich peat layers and their electron donor capacity for microbial activity and solute turnover processes.

2.2. Field and Lab Methods

We conducted the in situ measurements and core drillings with a Geoprobe 6610DT direct-push rig (*Kejr, Inc., USA*) at 35 locations within a 165 m × 130 m area at the boundary of the floodplain. For in situ color measurements to a depth of approximately 12 m, we used the soil color optical screening tool—SCOST (*Dakota Technologies Inc., USA*) as direct-push color logging probe (Dalan et al., 2011). This tool records

the visible light reflected from the sediments in XYZ color space with reference to the D65 white point of the CIE 1964 10° supplementary Standard Observer (Hausmann et al., 2016). We set the color acquisition frequency to two measurements per second; hence, the vertical resolution of the measurement depends on the rate of advancement. The median of the vertical resolution was 1.12 cm. Prior to each probing, we calibrated the color logging tool with acrylic color in mars black and titanium white (*Liquitex, Basics Acrylic*) with $L^* = 26.6$ and $L^* = 99.67$, respectively. For additional information on the tool, software, and internal signal processing, we refer to Dalan et al. (2011) and Hausmann et al. (2016). For method comparison, we also recorded vertical profiles of electrical conductivity and natural gamma radiation at one of the color logging locations. At this location (X112), we also retrieved a sediment core to compare the in situ colors to lab measurements and later took samples for TOC analysis. In the lab, we split off the upper third of the core lengthwise to create a fresh surface and avoid contamination from smearing effects along the inside of the plastic liner. We then covered the core with transparent plastic wrap and measured the sediment color with a Pausch color 5d handheld spectrophotometer *(Pausch Messtechnik GmbH, Germany)* three times per 1 cm depth interval to account for horizontal color variability. After these color measurements, we took 52 samples for subsequent TOC analysis. Again, the outer 1 cm of each sample was cut off to avoid cross contamination. These 52 and additional 47 sediment samples from nearby cores were dried and milled for homogenization. We then determined the TOC content of each sample by adding the TOC400 and ROC results from Elementar SoilTOC cube *(Elementar Analysesysteme GmbH, Germany)* three-staged loss on ignition measurements.

2.3. Data Processing

We translated the XYZ color data into the CIE $L^*a^*b^*$ color space. Subsequently, we fitted a Gaussian mixture model with three components to the merged set of CIE $L^*a^*b^*$ data of all in situ profiles using the function fitgmdist of the statistics and machine learning toolbox of Matlab (McLachlan & Peel, 2004). A Gaussian mixture model approximates the density of data points by the superposition of several multi-Gaussian distributions, each representing a cluster. In comparison to classical k-means clustering, Gaussian mixture models allow identifying clusters of points with different compactness and orientation in the parameter space. We give a more thorough explanation on the cluster analysis with Gaussian mixture models in Text S1 in the supporting information. The optimal number of clusters may be determined by application of information criteria (see Figure S2 in the supporting information). In our application, however, we chose the number of color clusters based on the best agreement with the lithological sequence reported for the Ammer valley sediments (Martin et al., 2020), resulting in three consistent clusters that can be related to a clay, peat, and autochthonous carbonate facies. That is, we dismissed a purely color-based distinction of more clusters that may have been justifiable by information criteria but did neither reflect comprehensible lithological differences nor improved the prediction of TOC content from the color classification. By fitting the Gaussian mixture model to the data, we assigned a membership probability for each of the three clusters, representing colorfacies, to each data point of each profile. For each data point we determined its most probable cluster membership and also evaluated the uncertainty of its assignment based on the membership probabilities for alternative clusters.

After cleaning the colorfacies profiles for outliers, we interpolated the contacts of the dominant colorfacies between the color log locations to visualize the three-dimensional colorfacies distribution along vertical cross sections. Finally, we fitted parametric functions to data from 99 sediment samples to predict their TOC content either from sediment lightness or a combination of lightness and chroma. Additionally, we separated the ranges of TOC content for each colorfacies and compared these to TOC ranges of lithofacies identified on the core.

3. Results and Discussion

Figure 1 shows a comparison of direct-push color measurements to other direct-push and downhole geophysical measurements, lithological descriptions, and handheld-spectrophotometer measurements on a drilling core. We performed the core drilling and reference geophysical measurements within 50 cm distance from the direct-push color log. We resampled all measurements to a vertical resolution of 1 cm by nearest-neighbor interpolation since the spectrophotometer measurements were performed in 1 cm intervals. We could distinguish the main lithofacies in a sedimentological core description as expected from

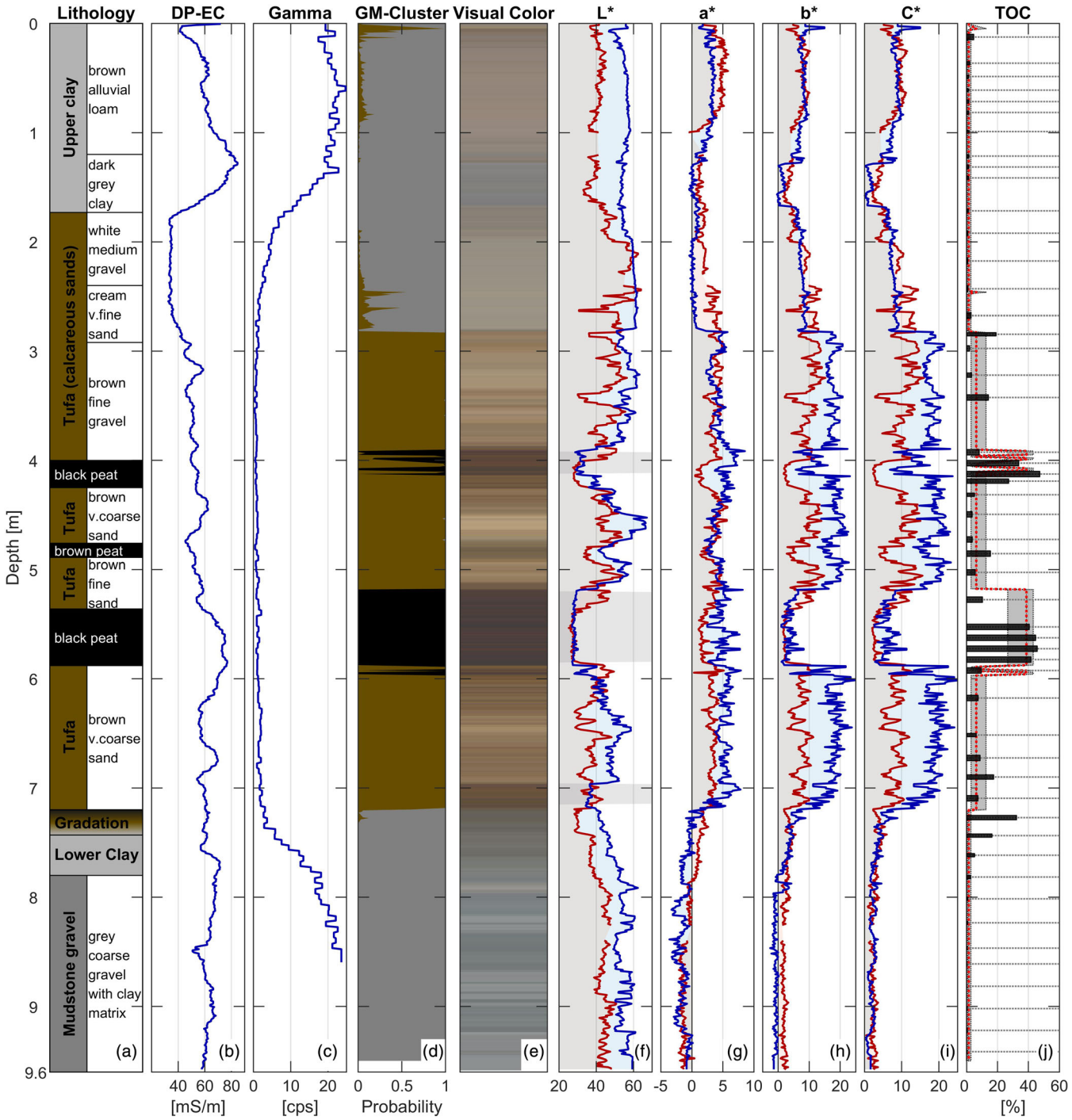

Figure 1. Example profiles of a floodplain sediment based on direct-push logging and sampling at location X112. From left to right: (a) lithology, (b) electric conductivity, (c) natural gamma ray emission, (d) probability of colorfacies membership by clustering using a Gaussian mixture model, (e) full color, (f–h) CIE $L^*a^*b^*$ channels (red: lab-based measurement on sediment core; blue: direct-push in situ measurement), (i) CIE chroma C*, (j) total organic carbon content in samples (black bars) and ranges predicted by the colorfacies.

preceding drillings (clayey gravel, lower clay, tufa, and upper silty clay) and determined two subfacies of the tufa, as well as three individual peat layers of 17, 40, and 22 cm thickness (Figure 1a).

The gray matrix-supported gravel at the bottom of the core contains mudstone clasts of up to 3 cm in an otherwise clayey matrix and upward grades into the lower gray clay similar to the gravel matrix. A subsequent upward gradation in color and texture forms the lithologic contact between gray silty clay at the

bottom and dark peaty silt on top at 7.43–7.2 m depth. This dark layer is the base of a 5.4 m thick calcareous tufa section with two subfacies: brown tufa with sand-sized grains, white tufa with gravel-sized grains, and peat. The brown tufa section contains an abundance of vegetation remnants between 7.2 and 2.92 m with two very dark peat layers at 4.0–4.25 and 5.36–5.88 m depth and a brown peat layer at 4.76–4.89 m. It is dominated by coarse sand to gravel-sized hollow cylinders of carbonates in a silty matrix. The upper section, the white gravely tufa (2.92–1.73 m), is composed of well-sorted cream to white calcareous tufa gravels with almost no vegetation remnants. Above, the upper clay shows a gray colored lower third between 1.73 and 1.2 m depth and a brownish upper section with roots and rare brick fragments in the uppermost 50 cm. The electric conductivity profile (Figure 1b) shows higher values in the upper 2 m, as well as at around 6 m depth, but shows otherwise no clear pattern. The natural gamma radiation measurements of six logging runs were averaged and reflect the abundance of radioactive ^{40}K with higher counts in the upper and lower clay and almost no signal within the tufa section (Figure 1c).

The in situ color measurement is presented in visual color as it would appear to an observer in Figure 1e and shows three main parts: a grayish-reddish upper section (0–2.9 m), a light to dark brown midsection (2.9–7.2 m), and a gray bottom section (7.2–9.6 m). The transition at 2.9 m is sharp, whereas the transition at 7.2 m depth appears downward gradational from brown to gray. Hence, both transitions match the described color changes of the core. Darker zones in the midsection are visible with relatively strong color contrast to the surrounding colors, whereas the lower clay and mudstone gravel are not distinguishable in the color log and hence are referred to as the lower gray section. The individual components of the CIE $L^*a^*b^*$ color space (blue lines in Figures 1f–1i) show more detail of the in situ color log. The sediment lightness L^* ranges between 26 and 60 with low a^* and b^* values in the gray sections and higher values in the brown section. The tufa lithology generally matches highest lightness and chroma values with strong vertical heterogeneity. Three box-shaped patterns are well distinguishable from 3.92–4.12, 5.2–5.85, and 6.96–7.15 m depth and internally consistent in low lightness (shaded zones in Figure 1f).

We compare these in situ color measurements with spectrophotometer measurements on the core (red lines) that show gaps where lost core hindered a continuous measurement. The general trend in sediment color matches well between in situ and ex situ measurements with comparably higher lightness and color saturation (chroma) measured under in situ conditions. However, the depth allocation and thickness of specific sections mismatches, that is, the dark section at ~5.5 m depth appears 15 cm higher and thicker in the in situ log than in the core and spectrophotometer log. Overall, these dark sections at 4, 5.5, and 7 m depth are located up to 20 cm higher and are up to 40% thicker in the in situ color log compared to the spectrophotometer measurements on the core. Finally, the 52 TOC samples from the core show relatively low values in the clay-rich upper and lower lithofacies, a fairly heterogeneous TOC distribution in the tufa section, and very high values in the peat layers (Figure 1j). Neither of the geophysical profiles correlates with the peat layers described on the core. Hence, the results presented in Figure 1 demonstrate the advantage of a continuous in situ color log of the subsurface to determine internal heterogeneity and depth allocations with high resolution where common in situ geophysical methods (i.e., electric conductivity and natural gamma ray logs) are not sensitive to targeted sedimentary changes. The comparison of the in situ direct-push color measurements to spectrophotometer measurements on the core validates the assumption that the probe was not affected by smearing effects, since color changes are sharp and located at higher positions in the direct-push color log. The peat layers were very soft and fully water saturated. Therefore, we interpret the offset in depth allocation and the decreased peat thickness in the core as a result of sediment compaction during the coring process. In addition, the lower lightness and chroma values on the core are probably due to the exposure of the previously fully saturated sediments to air in the lab and resulting changes in moisture content and chemical alterations. This is in accordance with studies showing a decrease in lightness within the first hours of drying for various saturated sediments (Lobell & Asner, 2002; Persson, 2005). Direct-push color logging hence minimizes common challenges in subsurface characterization from cores such as erroneous depth allocation due to compaction and poor core recovery, as well as sediment color alterations.

3.1. Spatial Mapping of Colorfacies

A highly resolved color log visualizes the vertical sediment heterogeneity yet makes it challenging to identify any other than the main lithological boundaries. In order to describe the 3-D subsurface architecture from all

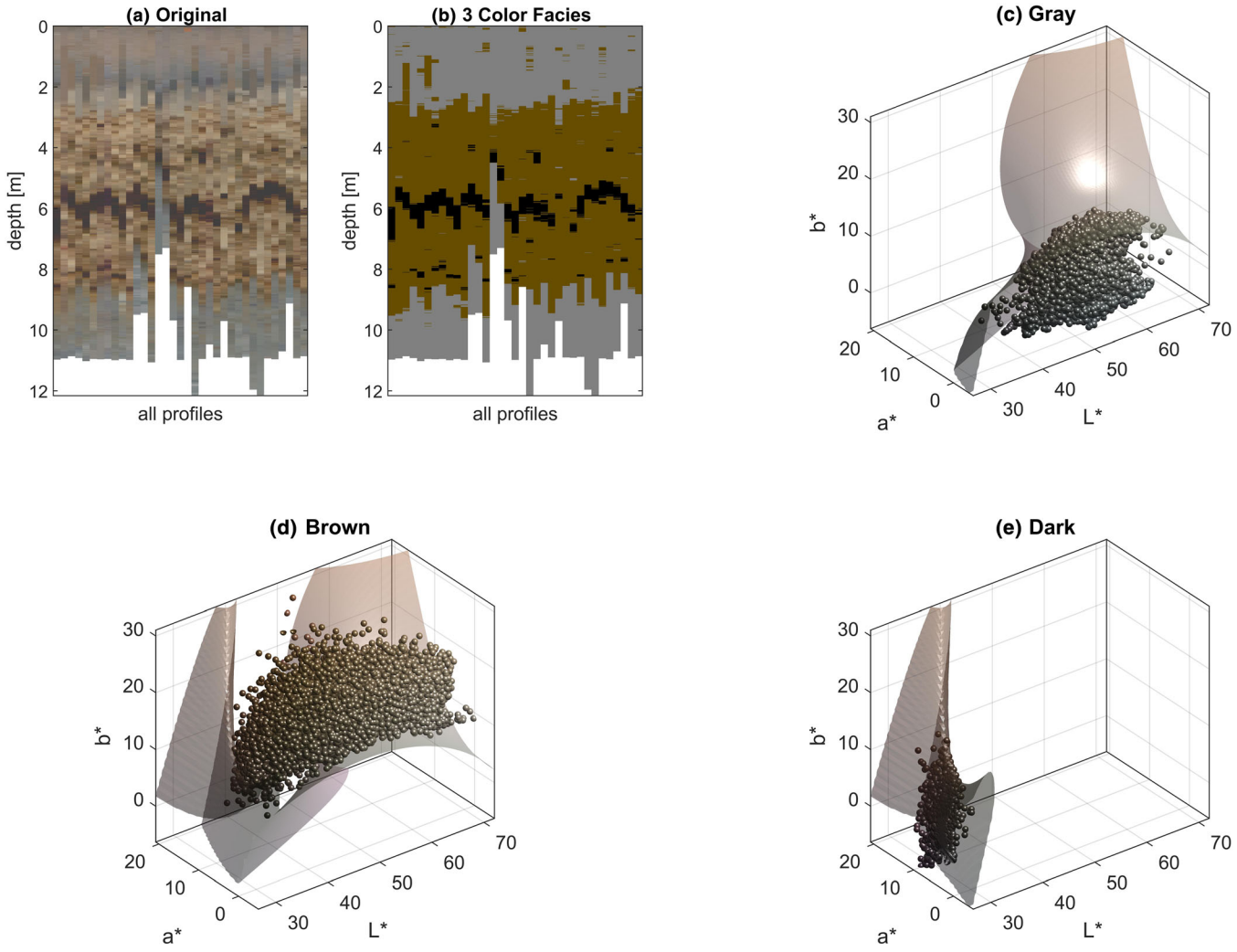

Figure 2. Cluster analysis of color profiles in CIE $L^*a^*b^*$ color space using a Gaussian mixture model. (a) All 35 original and (b) the resulting clustered color profiles. (c–e) Cluster bounding surface in CIE $L^*a^*b^*$ color space and all 36,903 individual measurements associated to the (c) gray, (d) brown, or (e) dark cluster. The colors in (b) differ from the mean $L^*a^*b^*$ values of the clusters, the scatter point shading in (c–e) shows the true measured sediment colors.

35 in situ color profiles, we focus on the main color contrasts and therefore assign all data points to either a gray, brown, or dark colorfacies by cluster analysis using a Gaussian mixture model applied to the color data in the CIE $L^*a^*b^*$ color space. We present a comparison of original and clustered color logs in Figures 2a and 2b and visualize the individual measurements per cluster in Figures 2c–2e. The supporting information includes the coefficients of each cluster obtained by the iterative Expectation-Maximization method (McLachlan & Peel, 2004) and the probabilities of each measurement point to belong to the individual clusters.

We identified a dark cluster of lower lightness, a gray cluster of a wide range of lightness but low chroma, and a brown cluster of a similar range of lightness yet higher chroma. In total, a fraction of 5.9% of the color measurements were classified as dark, 52.7% as brown, and 41.4% as gray colorfacies. A thick dark layer in 6 m depth and thinner dark layers at ≈4 and ≈8 m depth were resolved in almost all logging locations. The brown colorfacies is dominant between 2.5 and 9 m depth and bound by gray colorfacies on top and below. At first glance, the upper and lower clay-rich lithologies correlate to the gray colorfacies and are differentiated from both the tufa (brown) and peat (dark) sections. The upper gray section, however, also shows scattered brown patches in several color logs (Figure 2b).

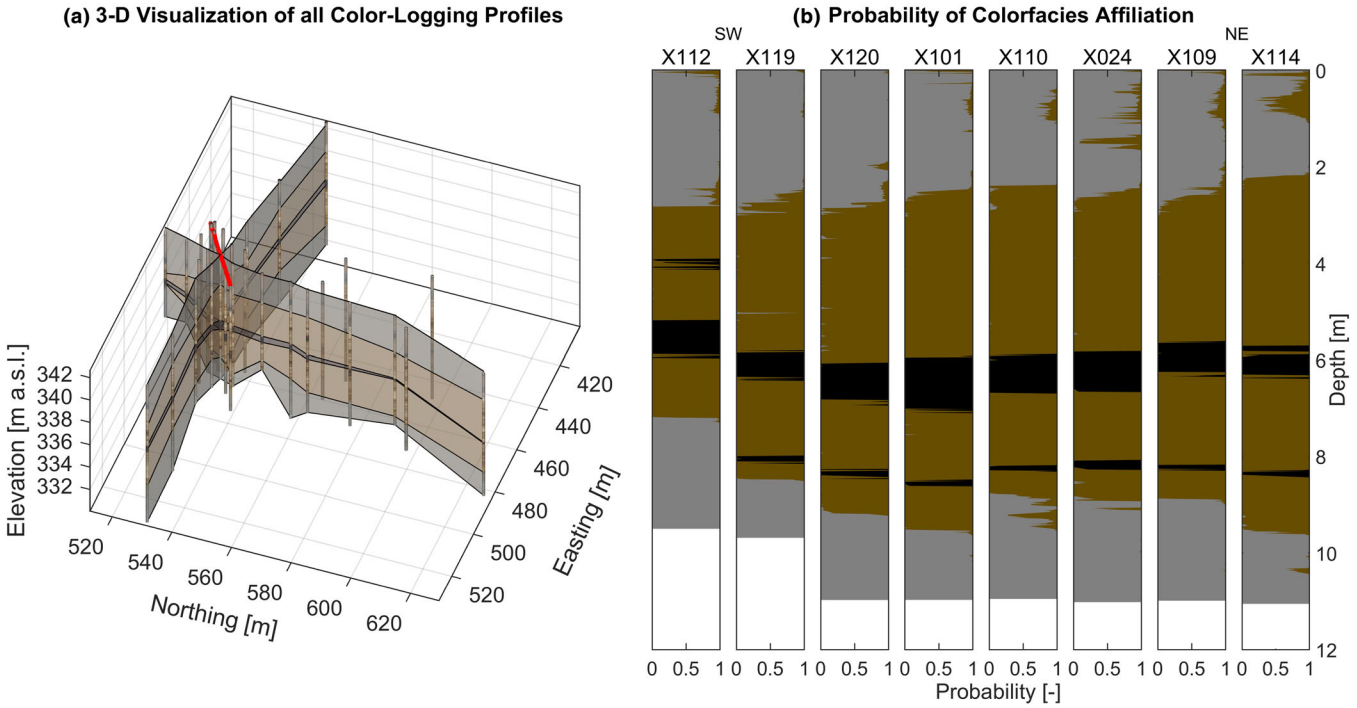

Figure 3. (a) Interpolated colorfacies boundaries between all 35 color logs. (b) Probability cross section along the red transect to visualize the uncertainty in cluster assignment within each log.

A more detailed comparison of the lithofacies and colorfacies in Figures 1a and 1d, respectively, shows that the upper, white to cream colored section of the tufa is clustered into the gray colorfacies down to the strong increase in chroma at 2.92 m depth. The color clustering obviously struggles with sediment colors plotting near the bounding surfaces of the colorfacies in Figures 2c–2e. The brown peat layer, for example, was clustered into the brown colorfacies since color logging is blind to sedimentary composition. The advantage of a cluster analysis with a Gaussian mixture model is the determined probability of each data point to belong to either of the individual clusters. Therefore, in contrast to assigning each data point to a unique colorfacies as in Figure 2b, we visualize the cummulative membership probabilities of the individual clusters in Figures 1d and 3b. This shows that most measurements were assigned a unique colorfacies with certainty (probability $\approx$1) resulting in mostly sharp contacts between the different colorfacies. Especially the upper gray colorfacies, however, additionally shows sections of nonunique cluster affiliations (0$\ll$ probability $\ll$1) where color measurements could be assigned to more than one of the three clusters depending on the individual membership probability. Measurements with an equal membership probability for two clusters plot on the bounding surface between the clusters visualized in Figures 2c–2e and show both colors at the same depth in Figures 1d and 3b. Significant membership probabilities for more than one colorfacies were assigned in the uppermost soil zone, as well as within the cream colored tufa. Such uncertain colorfacies memberships cause the patchy patterns in the upper 3 m of Figure 2b and need a careful interpretation with respect to their site-specific relevance.

To visualize the 3-D colorfacies distribution between all 35 color logs, we interpolated the spatial distribution of the main colorfacies over a 165 m $\times$ 130 m area in Figure 3a. We performed the direct-push color logs with larger spacings of 10–20 m along two main transects and refined the spacing close to their intersection down to 1.25 m between logging locations. The brown, tufa-related colorfacies is generally $\approx$6 m thick and thins out toward the south. The main target of color logging was the dark peat feature at $\approx$6 m depth, which continued over at least 135 m in the west-east direction and more than 100 m in the south-north direction. Along the diagonal and densely spaced transect, the main colorfacies contacts show similar depth allocations, while the thinner dark layers in 4 and 8 m depth do not fully extent over the entire transect (Figure 3b). As a result, we acquired a well-resolved image of the subsurface colorfacies distribution by direct-push color logging and could adaptively refine logging spacings to resolve the spatial extent of individual colorfacies.

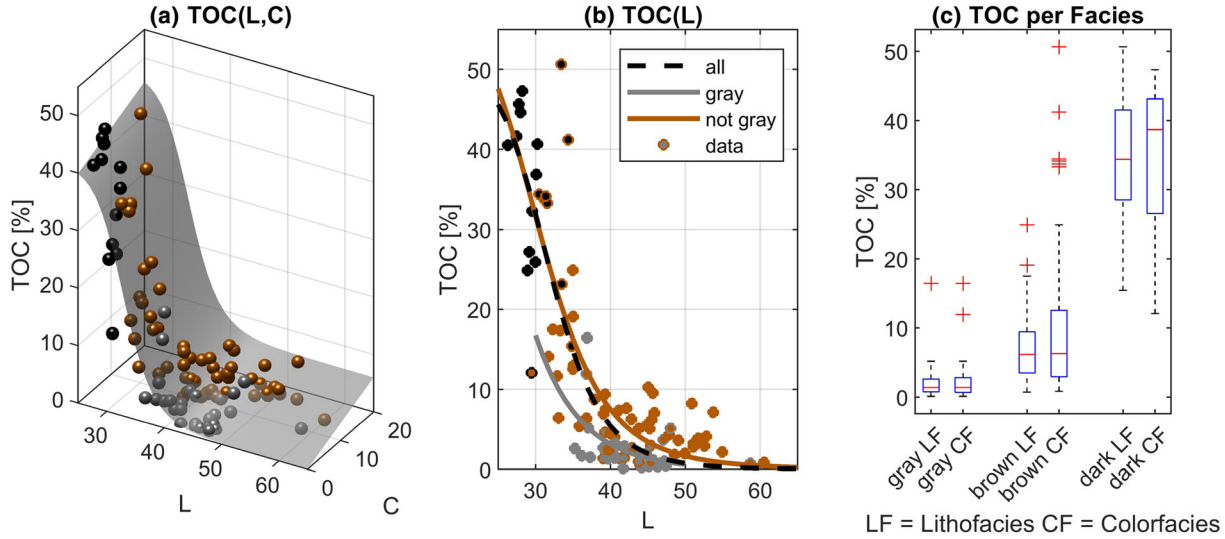

Figure 4. Relationship between sediment TOC content and spectrophotometer. (a) Lightness and chroma. (b) Lightness only, both for all data, as well as for gray and nongray colorfacies separately. (c) Median TOC value and ranges per colorfacies from the cluster analysis (CF) are comparable to those for lithofacies described on the core (LF).

3.2. TOC Estimation Using Sediment Colors

The potential of geochemically relevant features to function as hot spots for biogeochemical turnover and microbial activity depends on their spatial extent and TOC content. We thus analyzed a possible dependence of TOC content on sediment color. We established site-specific relationships between TOC content and spectrophotometer measurements from 52 samples from core location X112 and 47 additional samples from nearby core locations deriving different parametric functions. The TOC content of all samples ranged between ~50% in darker and 0.9% in lighter sediments.

After plotting the TOC content of each sample (TOC) as function of the spectrophotometer lightness L and chroma C (see Figure 4a), we fitted the following parametric surface to the data:

$$TOC(L,\ C) = TOC_{max}\left(1 - \frac{L^n}{L_{50}^n + L^n}\right) + s \times C, \tag{1}$$

in which the maximum TOC content TOC_{max} at zero chroma, half-lightness L_{50}, the exponent n, and the coefficient s relating the chroma to the TOC content were the fitting parameters. There is no physical reasoning for the specific parameterization of Equation 1 beyond expressing a negative, nonlinear influence of the lightness and a positive influence of the chroma on the estimated TOC content. The parametric fit is visualized by the gray surface in Figure 4a and describes the data with a root-mean-square error (RMSE) of 6.5% TOC. However, we achieved a similarly small RMSE value of 6.7% TOC by fitting the simpler dependency of TOC on the spectrophotometer lightness L only (Figure 4b, black dashed line) using the model:

$$TOC(L) = TOC_{max}\left(1 - \frac{L^n}{L_{50}^n + L^n}\right), \tag{2}$$

implying only a weak relationship between chroma and TOC content. In addition we also followed the suggestion of Liles et al. (2013) and tested independent parametric functions for preclustered samples. As the samples of the dark cluster did not show any clear dependence of the TOC content on either the lightness or the chroma, we merged it with the brown cluster, distinguishing now between gray and nongray samples. We fitted Equation 2 to the data points characterized as nongray (brown line in Figure 4b), and an exponential function to the data points belongs to the gray colorfacies (gray line in Figure 4b):

$$TOC(L) = TOC_{max} \times \exp\left(-\frac{L}{\lambda}\right), \quad (3)$$

yet could not significantly improve the RMSE (6.5% TOC). Optimal values for the fitting parameters TOC_{max},n,L_{50}, and s, as well as the correlation matrices and RMSE for each model, are given in the supporting information.

Instead of directly translating the color measurements into sediment TOC content, we rather acknowledge the uncertainty described by the RMSE and assign ranges of TOC content to each colorfacies. We present these ranges for all three main lithofacies (LF) described on the sediment core (Figure 1a), as well as the three colorfacies (CF) derived from the cluster analysis (Figure 1d) in Figure 4c. Median values and ranges of TOC content within facies, as well as the difference to other facies, are comparable between a lithology-based and a color-based classification. The few outliers mismatching in assigned colorfacies and lithofacies are indicated by the outer and inner marker colors in Figure 4b, respectively. Note that the medians and ranges of the box plots are also assigned to the full depth profile in Figure 1j.

The overall relationship between sediment color and TOC content described by the individual parametric functions is in accordance with the well-established relationship of higher TOC content in darker colored sediments and soils (Blume & Helsper, 1987; Gholizadeh et al., 2020; Konen et al., 2003; Liles et al., 2013). The reported fitting parameters for the chosen parametric functions, however, are very site specific and sample specific. The color measurements hence allow a generally applicable qualitative classification of zones with relatively higher and lower TOC content by darker and lighter sediment colors, respectively. Independent of the parametric model, however, the uncertainty in TOC prediction (RMSE of >6% TOC) is significantly high for lighter samples with <10% TOC. Especially internally heterogeneous samples with a dark surface on mainly light colored sediment and vice versa introduce errors since the color is only measured directly on the sample surface. Hence, centimeter-scale color changes from roots or vegetation remnants might be overinterpreted as spatially extensive variability of color and TOC content in the subsurface. Additionally, a direct translation from in situ colors to spectrophotometer measurements to predict TOC content may introduce errors due to previously discussed color alterations of the ex situ samples. We therefore rather assign ranges of TOC content to the previously identified colorfacies which proved to be comparable to ranges of TOC content for the described lithofacies. This allows a sound assessment of the potential relevance of individual spatially extensive colorfacies to microbial activity and pollutant turnover processes based on their median TOC content. In contrast to a lithology-based site characterization from drilling cores, the direct-push color logging method is quicker, less invasive, and more accurate in layer thickness and depth especially for the targeted soft and TOC-rich peats.

4. Conclusions

Measuring in situ sediment color to depths of 12 m at densely spaced direct-push logging locations provides a so far unmet image of the subsurface structure and heterogeneity. We classified site-specific colorfacies and mapped their extent and contacts at a depth-independent centimeter-scale resolution over 160 × 135 m. The cluster analysis by Gaussian mixture models led to individual colorfacies agreeing well with independently determined lithofacies. The in situ color logging is less invasive and much faster than a site characterization based on few costly drillings and even more accurate when assessing thickness and depth allocation of targeted color zones. In addition, the color logging results may serve as basis for a subsequent excavation or coring campaign with precisely targeted sampling. For biogeochemical applications, the site-specific relationships between TOC content and sediment color from few cores allow a direct mapping of the TOC distribution in the subsurface. Considering the uncertainty in predicting TOC content for lighter samples, however, we recommend using ranges of TOC content for each colorfacies instead. These ranges proved to be comparable to those of the associated lithofacies described from a drilling core. Among the geophysical logs applied in this study, only color logging was indicative of the TOC content. Considering literature reports on using CPT to identify peat layers (Boylan & Long, 2012; Tumay et al., 2013) leads to the suggestion of comparing or combining CPT and color logs as proxy for the TOC content in future work.

In the present study we used the direct-push based colorfacies delineation only to identify zones of high TOC in the subsurface. The method, however, may be used for various other applications, such as mapping the iron content and redox conditions in soil science and biogeochemistry, logging seasonal cyclicity in paleoenvironmental studies, chasing optical tracers in hydrogeology, or detecting archeological structures and sedimentary features.

Data Availability Statement

The data of the color-logs and cores as well as the matlab files used for the analysis are published in the database of the project "CAMPOS - Catchments as Reactors" at the University of Tübingen, available online (http://hdl.handle.net/10900.1/8687010a-86e8-43cb-9999-7d7171e463f5).

Acknowledgments
This study is supported by the German Research Foundation (Deutsche Forschungsgemeinschaft, DFG) by the Collaborative Research Center SFB 1253 "CAMPOS-Catchments as Reactors", project P3: "Structural Controls of the Hydrological Functioning of a Floodplain". We thank M. Kreck and A. Schoßland (UFZ Leipzig) for their support in the field, L. Herrmann and D. Frobel (University of Hohenheim) and B. Nisch (University Tübingen) for their lab support, and T. Rotava and K. Singer for lab work. Finally, we thank the three anonymous reviewers for their helpful comments on the paper. Open access funding enabled and organized by Projekt DEAL.

References

Ackerson, J. P., Morgan, C. L. S., & Ge, Y. (2017). Penetrometer-mounted VisNIR spectroscopy: Application of EPO-PLS to in situ VisNIR spectra. *Geoderma*, *286*, 131–138. https://doi.org/10.1016/j.geoderma.2016.10.018

Adamchuk, V. I., Hummel, J. W., Morgan, M. T., & Upadhyaya, S. K. (2004). On-the-go soil sensors for precision agriculture. *Computers and Electronics in Agriculture*, *44*(1), 71–91. https://doi.org/10.1016/j.compag.2004.03.002

Aitkenhead, M. J., Coull, M., Towers, W., Hudson, G., & Black, H. I. J. (2013). Prediction of soil characteristics and colour using data from the National Soils Inventory of Scotland. *Geoderma*, *200–201*, 99–107. https://doi.org/10.1016/j.geoderma.2013.02.013

Aliah Baharom, S. N., Shibusawa, S., Kodaira, M., & Kanda, R. (2015). Multiple-depth mapping of soil properties using a visible and near infrared real-time soil sensor for a paddy field, *Engineering in Agriculture. Environment and Food*, *8*(1), 13–17. https://doi.org/10.1016/j.eaef.2015.01.002

Barron, V., & Torrent, J. (1986). Use of the Kubelka-Munk theory to study the influence of iron oxides on soil colour. *Journal of Soil Science*, *37*(4), 499–510. https://doi.org/10.1111/j.1365-2389.1986.tb00382.x

Bauer, I., & Kappler, A. (2009). Rates and extent of reduction of Fe (III) compounds and O_2 by humic substances. *Environmental Science & Technology*, *43*(13), 4902–4908. https://doi.org/10.1021/es900179s

Blume, H.-P., & Helsper, M. (1987). Schätzung des Humusgehaltes nach der Munsell-Farbhelligkeit. *Zeitschrift für Pflanzenernährung und Bodenkunde*, *150*(5), 354–356. https://doi.org/10.1002/jpln.19871500515

Boylan, N., & Long, M. (2012). In situ testing of peat—A review and update on recent developments. *Geotechnical Engineering Journal of the SEAGS & AGSSEA*, *43*(4), 41–55.

Bujewski, G. R., & Rutherford, B. (1997). The rapid optical screeining tool (ROST) laser-induced flourescence screening system for screening petroleum hydrocarbons in subsurface soils, *EPA Report EPA/600/R-97/020*.

CIE (1978). Supplement 2 to CIE publication 15 (E1.3.1) 1971/(TC1.3): Recommendations on uniform color spaces, color-difference equations, psychometric color terms, *Commission Internationale de l'Éclairage (Vienna, Austria)*.

Comas, X., Terry, N., Hribljan, J. A., Lilleskov, E. A., Suarez, E., Chimner, R. A., & Kolka, R. K. (2017). Estimating belowground carbon stocks in peatlands of the Ecuadorian páramo using ground-penetrating radar (GPR). *Journal of Geophysical Research: Biogeosciences*, *122*, 370–386. https://doi.org/10.1002/2016jg003550

Comas, X., Terry, N., Slater, L., Warren, M., Kolka, R., Kristiyono, A., et al. (2015). Imaging tropical peatlands in Indonesia using ground-penetrating radar (GPR) and electrical resistivity imaging (ERI): Implications for carbon stock estimates and peat soil characterization. *Biogeosciences*, *12*(10), 2995–3007. https://doi.org/10.5194/bg-12-2995-2015

Corradini, E., Wilken, D., Zanon, M., Groß, D., Lübke, H., Panning, D., et al. (2020). Reconstructing the palaeoenvironment at the early Mesolithic site of Lake Duvensee: Ground-penetrating radar and geoarchaeology for 3D facies mapping. *The Holocene*, *30*(6), 820–833. https://doi.org/10.1177/0959683620902234

Dabkowski, J. (2020). The late-Holocene tufa decline in Europe: Myth or reality? *Quaternary Science Reviews*, *230*, 106141. https://doi.org/10.1016/j.quascirev.2019.106141

Dalan, R. A., Bevan, B. W., Goodman, D., Lynch, D., De Vore, S., Adamek, S., et al. (2011). The measurement and analysis of depth in archaeological geophysics: Tests at the Biesterfeldt site, USA. *Archaeological Prospection*, *18*(4), 245–265. https://doi.org/10.1002/arp.419

Doetterl, S., Stevens, A., Van Oost, K., & van Wesemael, B. (2013). Soil organic carbon assessment at high vertical resolution using closed-tube sampling and Vis-NIR spectroscopy. *Soil Science Society of America Journal*, *77*(4), 1430–1435. https://doi.org/10.2136/sssaj2012.0410n

Dorador, J., & Rodríguez-Tovar, F. J. (2016). High resolution digital image treatment to color analysis on cores from IODP Expedition 339: Approaching lithologic features and bioturbational influence. *Marine Geology*, *377*, 127–135. https://doi.org/10.1016/j.margeo.2016.02.005

Einarson, M., Fure, A., Germain, R. S., Chapman, S., & Parker, B. (2018). DyeLIF™: A new direct-push laser-induced fluorescence sensor system for chlorinated solvent DNAPL and other non-naturally fluorescing NAPLs. *Groundwater Monitoring & Remediation*, *38*(3), 28–42. https://doi.org/10.1111/gwmr.12296

Fuchs, M., Will, M., Kunert, E., Kreutzer, S., Fischer, M., & Reverman, R. (2011). The temporal and spatial quantification of Holocene sediment dynamics in a meso-scale catchment in northern Bavaria, Germany. *The Holocene*, *21*(7), 1093–1104. https://doi.org/10.1177/0959683611400459

Gholizadeh, A., Saberioon, M., Viscarra Rossel, R. A., Boruvka, L., & Klement, A. (2020). Spectroscopic measurements and imaging of soil colour for field scale estimation of soil organic carbon. *Geoderma*, *357*, 113972. https://doi.org/10.1016/j.geoderma.2019.113972

Glodowska, M., Stopelli, E., Schneider, M., Lightfoot, A., Rathi, B., Straub, D., et al. (2020). Role of in situ natural organic matter in mobilizing as during microbial reduction of Fe (III)-mineral-bearing aquifer sediments from Hanoi (Vietnam). *Environmental Science & Technology*, *54*(7), 4149–4159. https://doi.org/10.1021/acs.est.9b07183

Hartemink, A. E., & Minasny, B. (2014). Towards digital soil morphometrics. *Geoderma*, *230–231*, 305–317. https://doi.org/10.1016/j.geoderma.2014.03.008

Hausmann, J., Dietrich, P., Vienken, T., & Werban, U. (2016). Technique, analysis routines, and application of direct push-driven in situ color logging. *Environmental Earth Sciences*, *75*, 957. https://doi.org/10.1007/s12665-016-5515-7

Hausmann, J., Zielhofer, C., Werther, L., Berg-Hobohm, S., Dietrich, P., Heymann, R., & Werban, U. (2018). Direct push sensing in wetland (geo)archaeology: High-resolution reconstruction of buried canal structures (Fossa Carolina, Germany). *Quaternary International*, *473*, 21–36. https://doi.org/10.1016/j.quaint.2017.02.008

Heil, J., Marschner, B., & Stumpe, B. (2020). Digital photography as a tool for microscale mapping of soil organic carbon and iron oxides. *Catena*, *193*, 104610. https://doi.org/10.1016/j.catena.2020.104610

Kalbitz, K., & Wennrich, R. (1998). Mobilization of heavy metals and arsenic in polluted wetland soils and its dependence on dissolved organic matter. *Science of the Total Environment*, *209*(1), 27–39. https://doi.org/10.1016/s0048-9697(97)00302-1

Kettridge, N., Comas, X., Baird, A., Slater, L., Strack, M., Thompson, D., et al. (2008). Ecohydrologically important subsurface structures in peatlands revealed by ground-penetrating radar and complex conductivity surveys. *Journal of Geophysical Research*, *113*, G04030. https://doi.org/10.1029/2008jg000787

Knadel, M., Thomsen, A., Schelde, K., & Greve, M. H. (2015). Soil organic carbon and particle sizes mapping using vis–NIR, EC and temperature mobile sensor platform. *Computers and Electronics in Agriculture*, *114*, 134–144. https://doi.org/10.1016/j.compag.2015.03.013

Konen, M. E., Burras, C. L., & Sandor, J. A. (2003). Organic carbon, texture, and quantitative color measurement relationships for cultivated soils in north Central Iowa. *Soil Science Society of America Journal*, *67*(6), 1823–1830. https://doi.org/10.2136/sssaj2003.1823

Korom, S. F. (1992). Natural denitrification in the saturated zone: A review. *Water Resources Research*, *28*(6), 1657–1668. https://doi.org/10.1029/92wr00252

Kowalczyk, S., Żukowska, K. A., Mendecki, M. J., & Łukasiak, D. (2017). Application of electrical resistivity imaging (ERI) for the assessment of peat properties: A case study of the Całowanie Fen, Central Poland. *Acta Geophysica*, *65*(1), 223–235. https://doi.org/10.1007/s11600-017-0018-9

Kram, M. L., Lieberman, S. H., Fee, J., & Keller, A. A. (2001). Use of LIF for real-time in-situ mixed NAPL source zone detection. *Groundwater Monitoring & Remediation*, *21*(1), 67–76. https://doi.org/10.1111/j.1745-6592.2001.tb00632.x

Lawson, M., Polya, D. A., Boyce, A. J., Bryant, C., & Ballentine, C. J. (2016). Tracing organic matter composition and distribution and its role on arsenic release in shallow Cambodian groundwaters. *Geochimica et Cosmochimica Acta*, *178*, 160–177. https://doi.org/10.1016/j.gca.2016.01.010

Lespez, L., Clet-Pellerin, M., Limondin-Lozouet, N., Pastre, J.-F., Fontugne, M., & Marcigny, C. (2008). Fluvial system evolution and environmental changes during the Holocene in the Mue valley (Western France). *Geomorphology*, *98*(1–2), 55–70. https://doi.org/10.1016/j.geomorph.2007.02.029

Liles, G. C., Beaudette, D. E., O'Geen, A. T., & Horwath, W. R. (2013). Developing predictive soil C models for soils using quantitative color measurements. *Soil Science Society of America Journal*, *77*(6), 2173–2181. https://doi.org/10.2136/sssaj2013.02.0057

Lobell, D. B., & Asner, G. P. (2002). Moisture effects on soil reflectance. *Soil Science Society of America Journal*, *66*(3), 722–727. https://doi.org/10.2136/sssaj2002.7220

Lunne, T., Powell, J. J., & Robertson, P. K. (2002). *Cone penetration testing in geotechnical practice* (1st ed.). London: CRC Press. https://doi.org/10.1201/9781482295047

Lyle, M. (1983). The brown-green color transition in marine sediments: A marker of the Fe (III)-Fe (II) redox boundary1. *Limnology and Oceanography*, *28*(5), 1026–1033. https://doi.org/10.4319/lo.1983.28.5.1026

Martin, S., Klingler, S., Dietrich, P., Leven, C., & Cirpka, O. A. (2020). Structural controls on the hydrogeological functioning of a floodplain. *Hydrogeology Journal*, *28*(8), 2675–2696. https://doi.org/10.1007/s10040-020-02225-8

McArthur, J. M., Banerjee, D. M., Hudson-Edwards, K. A., Mishra, R., Purohit, R., Ravenscroft, P., et al. (2004). Natural organic matter in sedimentary basins and its relation to arsenic in anoxic ground water: The example of West Bengal and its worldwide implications. *Applied Geochemistry*, *19*(8), 1255–1293. https://doi.org/10.1016/j.apgeochem.2004.02.001

McCall, W., Christy, T. M., Pipp, D. A., Jaster, B., White, J., Goodrich, J., et al. (2018). Evaluation and application of the optical image profiler (OIP) a direct push probe for photo-logging UV-induced fluorescence of petroleum hydrocarbons. *Environmental Earth Sciences*, *77*, 374. https://doi.org/10.1007/s12665-018-7442-2

McLachlan, G. J., & Peel, D. (2004). *Finite Mixture Models*, *Wiley series in probability and statistics. Applied probability and statistics section*. New York: John Wiley & Sons.

Melville, M. D., & Atkinson, G. (1985). Soil colour: Its measurement and its designation in models of uniform colour space. *Journal of Soil Science*, *36*(4), 495–512. https://doi.org/10.1111/j.1365-2389.1985.tb00353.x

Morgan, C. L. S., Waiser, T. H., Brown, D. J., & Hallmark, C. T. (2009). Simulated in situ characterization of soil organic and inorganic carbon with visible near-infrared diffuse reflectance spectroscopy. *Geoderma*, *151*(3–4), 249–256. https://doi.org/10.1016/j.geoderma.2009.04.010

Moritsuka, N., Kawamura, K., Tsujimoto, Y., Rabenarivo, M., Andriamananjara, A., Rakotoson, T., & Razafimbelo, T. (2019). Comparison of visual and instrumental measurements of soil color with different low-cost colorimeters. *Soil Science and Plant Nutrition*, *65*(6), 605–615. https://doi.org/10.1080/00380768.2019.1676624

Nederbragt, A. J., & Thurow, J. W. (2001). A 6000 yr varve record of Holocene climate in Saanich Inlet, British Columbia, from digital sediment colour analysis of ODP Leg 169S cores. *Marine Geology*, *174*(1–4), 95–110. https://doi.org/10.1016/S0025-3227(00)00144-4

Newell, A. J., Sorensen, J. P. R., Chambers, J. E., Wilkinson, P. B., Uhlemann, S., Roberts, C., et al. (2015). Fluvial response to Late Pleistocene and Holocene environmental change in a Thames chalkland headwater: The Lambourn of southern England. *Proceedings of the Geologists Association*, *126*(6), 683–697. https://doi.org/10.1016/j.pgeola.2015.08.008

Passey, Q. R., Creaney, S., Kulla, J. B., Moretti, F. J., & Stroud, J. D. (1990). A practical model for organic richness from porosity and resistivity logs. *AAPG Bulletin-American Association of Petroleum Geologists*, *74*(12), 1777–1794. https://doi.org/10.1306/0c9b25c9-1710-11d7-8645000102c1865d

Pedley, H. M. (1990). Classification and environmental models of cool freshwater tufas. *Sedimentary Geology*, *68*(1–2), 143–154. https://doi.org/10.1016/0037-0738(90)90124-c

Persson, M. (2005). Estimating surface soil moisture from soil color using image analysis. *Vadose Zone Journal*, *4*(4), 1119–1122. https://doi.org/10.2136/vzj2005.0023

Peterson, L. C., Haug, G. H., Hughen, K. A., & Rohl, U. (2000). Rapid changes in the hydrologic cycle of the tropical Atlantic during the last glacial. *Science*, *290*(5498), 1947–1951. https://doi.org/10.1126/science.290.5498.1947

Poggio, M., Brown, D. J., & Bricklemyer, R. S. (2015). Laboratory-based evaluation of optical performance for a new soil penetrometer visible and near-infrared (VisNIR) foreoptic. *Computers and Electronics in Agriculture*, *115*, 12–20. https://doi.org/10.1016/j.compag.2015.05.002

Rabiger-Völlmer, J., Schmidt, J., Linzen, S., Schneider, M., Werban, U., Dietrich, P., et al. (2020). Non-invasive prospection techniques and direct push sensing as high-resolution validation tools in wetland geoarchaeology—Artificial water supply at a Carolingian canal in South Germany? *Journal of Applied Geophysics*, *173*, 103928. https://doi.org/10.1016/j.jappgeo.2019.103928

Reischer, M., Christensen, A. G., De Weirdt, F., Bruns, S., & Dideriksen, K. (2020). Capabilities of an optical direct push probe for 2D-subsurface imaging. *Journal of Contaminant Hydrology*, *232*, 103636. https://doi.org/10.1016/j.jconhyd.2020.103636

Rivett, M. O., Buss, S. R., Morgan, P., Smith, J. W., & Bemment, C. D. (2008). Nitrate attenuation in groundwater: A review of biogeochemical controlling processes. *Water Research*, *42*(16), 4215–4232. https://doi.org/10.1016/j.watres.2008.07.020

Rodionov, A., Welp, G., Damerow, L., Berg, T., Amelung, W., & Pätzold, S. (2015). Towards on-the-go field assessment of soil organic carbon using Vis–NIR diffuse reflectance spectroscopy: Developing and testing a novel tractor-driven measuring chamber. *Soil and Tillage Research*, *145*, 93–102. https://doi.org/10.1016/j.still.2014.08.007

Scheinost, A. C., & Schwertmann, U. (1999). Color identification of iron oxides and hydroxysulfates. *Soil Science Society of America Journal*, *63*(5), 1463–1471. https://doi.org/10.2136/sssaj1999.6351463x

Silvestri, S., Christensen, C. W., Lysdahl, A. O. K., Anschütz, H., Pfaffhuber, A. A., & Viezzoli, A. (2019). Peatland volume mapping over resistive substrates with airborne electromagnetic technology. *Geophysical Research Letters*, *46*, 6459–6468. https://doi.org/10.1029/2019gl083025

Slater, L. D., & Reeve, A. (2002). Investigating peatland stratigraphy and hydrogeology using integrated electrical geophysics. *Geophysics*, *67*(2), 365–378. https://doi.org/10.1190/1.1468597

Spielvogel, S., Knicker, H., & Kögel-Knabner, I. (2004). Soil organic matter composition and soil lightness. *Journal of Plant Nutrition and Soil Science*, *167*(5), 545–555. https://doi.org/10.1002/jpln.200421424

Steinhardt, G. C., & Franzmeier, D. P. (2008). Comparison of organic matter content with soil color for silt loam soils of Indiana. *Communications in Soil Science and Plant Analysis*, *10*(10), 1271–1277. https://doi.org/10.1080/00103627909366981

Torrent, J., Schwertmann, U., Fechter, H., & Alferez, F. (1983). Quantitative relationships between soil color and hematite content. *Soil Science*, *136*(6), 354–358. https://doi.org/10.1097/00010694-198312000-00004

Tumay, M., Hatipkarasulu, Y., Marx, E., & Cotton, B. (2013). CPT/PCPT-based organic material profiling, paper presented at Proc. 18th Intl. Conf. on soil mechanics & geotechnical engineering.

Veum, K. S., Parker, P. A., Sudduth, K. A., & Holan, S. H. (2018). Predicting profile soil properties with reflectance spectra via Bayesian covariate-assisted external parameter orthogonalization. *Sensors (Basel)*, *18*, 3869. https://doi.org/10.3390/s18113869

Viscarra Rossel, R. A., Cattle, S. R., Ortega, A., & Fouad, Y. (2009). In situ measurements of soil colour, mineral composition and clay content by vis–NIR spectroscopy. *Geoderma*, *150*(3–4), 253–266. https://doi.org/10.1016/j.geoderma.2009.01.025

Viscarra Rossel, R. A., Minasny, B., Roudier, P., & McBratney, A. B. (2006a). Colour space models for soil science. *Geoderma*, *133*(3–4), 320–337. https://doi.org/10.1016/j.geoderma.2005.07.017

Viscarra Rossel, R. A., Walvoort, D. J. J., McBratney, A. B., Janik, L. J., & Skjemstad, J. O. (2006b). Visible, near infrared, mid infrared or combined diffuse reflectance spectroscopy for simultaneous assessment of various soil properties. *Geoderma*, *131*(1–2), 59–75. https://doi.org/10.1016/j.geoderma.2005.03.007

Waiser, T. H., Morgan, C. L. S., Brown, D. J., & Hallmark, C. T. (2007). In situ characterization of soil clay content with visible near-infrared diffuse reflectance spectroscopy. *Soil Science Society of America Journal*, *71*(2), 389–396. https://doi.org/10.2136/sssaj2006.0211

Wijewardane, N. K., Hetrick, S., Ackerson, J., Morgan, C. L. S., & Ge, Y. (2020). VisNIR integrated multi-sensing penetrometer for in situ high-resolution vertical soil sensing. *Soil and Tillage Research*, *199*, 104604. https://doi.org/10.1016/j.still.2020.104604

Wills, S. A., Burras, C. L., & Sandor, J. A. (2007). Prediction of soil organic carbon content using field and laboratory measurements of soil color. *Soil Science Society of America Journal*, *71*(2), 380–388. https://doi.org/10.2136/sssaj2005.0384

Žák, K., Ložek, V., Kadlec, J., Hladíková, J., & Cílek, V. (2002). Climate-induced changes in Holocene calcareous tufa formations, Bohemian Karst, Czech Republic. *Quaternary International*, *91*(1), 137–152. https://doi.org/10.1016/s1040-6182(01)00107-0

Zhang, Y., Biswas, A., Ji, W., & Adamchuk, V. I. (2017). Depth-specific prediction of soil properties in situ using vis-NIR spectroscopy. *Soil Science Society of America Journal*, *81*(5), 993–1004. https://doi.org/10.2136/sssaj2016.08.0253

Zhang, Y., & Hartemink, A. E. (2019a). Digital mapping of a soil profile. *European Journal of Soil Science*, *70*(1), 27–41. https://doi.org/10.1111/ejss.12699

Zhang, Y., & Hartemink, A. E. (2019b). Soil horizon delineation using vis-NIR and pXRF data. *Catena*, *180*, 298–308. https://doi.org/10.1016/j.catena.2019.05.001

Zhu, L., Zhang, C., Zhang, C., Zhang, Z., Zhou, X., Liu, W., & Zhu, B. (2020). A new and reliable dual model- and data-driven TOC prediction concept: A TOC logging evaluation method using multiple overlapping methods integrated with semi-supervised deep learning. *Journal of Petroleum Science and Engineering*, *188*, 106944. https://doi.org/10.1016/j.petrol.2020.106944

Zolitschka, B., Francus, P., Ojala, A. E. K., & Schimmelmann, A. (2015). Varves in lake sediments—A review. *Quaternary Science Reviews*, *117*, 1–41. https://doi.org/10.1016/j.quascirev.2015.03.019

References From the Supporting Information

Dempster, A. P., Laird, N. M., & Rubin, D. B. (1977). Maximum likelihood from incomplete data via the EM algorithm. *Journal of the Royal Statistical Society: Series B: Methodological*, *39*(1), 1–22.